Improvement Torque Performances of Interior Permanent-Magnet Machines

Junqiang Zheng, Wenxiang Zhao, *Senior Member*, *IEEE*, Christopher H. T. Lee, *Senior Member, IEEE*, Jinghua Ji and Gaohong Xu
(Invited)

***Abstract*—Due to their excellent efficiency, power density and constant power speed region, interior permanent-magnet (IPM) machines are very suitable for electric vehicles (EVs). This paper proposed a new IPM rotor topology, which can offer high reluctance torque, wide constant power speed range and excellent overload capability. Besides, five rotor topologies with integral-slot distributed-windings IPM machines, including four existing IPM topologies and the proposed IPM topology, are designed optimally. Their characteristics, which include *d-q* axis inductances, saliency ratios, electromagnetic torques, corresponding torque ripples, back-electromotive forces (EMFs), overload capabilities and flux weakening performances are evaluated quantitatively. Finally, a three phase 48s8p hybrid rotor PM machine is built to verify the performances of the proposed IPM machine. This work provides some general concepts for machine developers who are willing to build IPM machines for high-performance EV applications.**

***Index Terms*—Flux weakening, finite-element analysis (FEA), interior permanent-magnet brushless machine, reluctance torque, inductance.**

I. Introduction

DUE TO these advantages, including excellent torque and power densities, flux weakening performance and efficiency, interior permanent-magnet (IPM) machines have attracted more attentions for traction applications, e.g., electric vehicles (EVs) and hybrid electric vehicles (HEVs) [1]-[3]. Based on the asymmetry of *d-q* axis magnetic circuit, IPM machine with distributed windings can generate high reluctance torque. It is indispensable to point out that reluctance torque can greatly increase output torque and improve flux weakening capability for IPM machines [4], [5]. The output torque of IPM machine can be roughly classified by two parts, namely PM torque and reluctance torque. In particular, the PM torque is developed based on interaction between air-gap magnetic field and stator armature reaction magnetic field, while the reluctance torque is instead on asymmetry between magnetic circuit of *d*-axis and *q*-axis [6]-[10]. The PM field promotes a safety hazard when machines stop quickly or idle running. To relieve this risk, the amplitude of the back-electromotive forces (EMFs) must be retained within a threshold value. Thus, PM torque component should be limited so as its output torque. When EVs undergoes for a high speed operation, utilization of reluctance torque and flux weakening capability become very important [11]-[14]. However, the detailed comparisons among IPM machines with different rotor topologies are literally absent yet.

This paper proposes a new IPM rotor topology to improve reluctance torque value, flux weakening performance and overload capability. First, five IPM machine with different rotor structures are developed and compared fairly. Second, their electromagnetic characteristics, including *d-q* axis inductances, saliency ratios, electromagnetic torques, corresponding torque ripples, back-EMFs, overload capabilities and flux weakening performances, are evaluated quantitatively. This work provides some general concepts for machine designers who are willing to build IPM machines for high-performance EV applications.

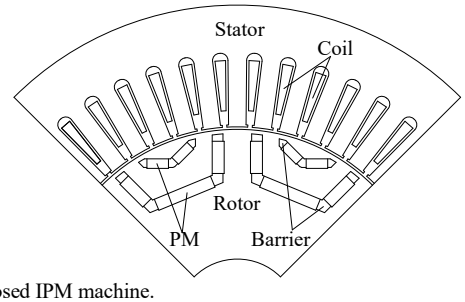

Fig. 1. Proposed IPM machine.

II. Proposed IPM Machine

Fig. 1 presents the rotor topology of the proposed IPM machine. As shown, the proposed machine is installed with two types of PMs, namely U-shape and V-shape, while the interval between two types of PMs is relatively large. This particular layout, namely double layers of PMs design can maximize the reluctance torque. The size and position of all PM material have been analyzed to produce a satisfactory reluctance torque. The number of span of the windings is selected to be six. In order to avoid local magnetic saturation and to achieve good overload capability, stator tooth and yoke have been enlarged in purpose.

Simplified equivalent *d-q* axis armature reaction magnetic circuit of the proposed IPM machine is exhibited in Fig. 2. It

Manuscript was submitted for review on 17, January, 2019.
This work was supported by the Key Research and Development Program of Jiangsu Province (BE2018107), and by the Six Talent Peaks Project of Jiangsu Province (2017-KTHY-011), and by the Graduate Scientific Research Innovation Project of Jiangsu Province (KYCX18_2248).
J. Zheng, W. Zhao, J. Ji and G. Xu are with School of Electrical and Information Engineering, Jiangsu University, Zhenjiang 212013, China (zwx@ujs.edu.cn).
C. H. T. Lee is with the School of Electrical and Electronic Engineering, Nanyang Technological University, Singapore (e-mail: chtlee@ntu.edu.sg).
Digital Object Identifier 10.30941/CESTEMS.2019.00003

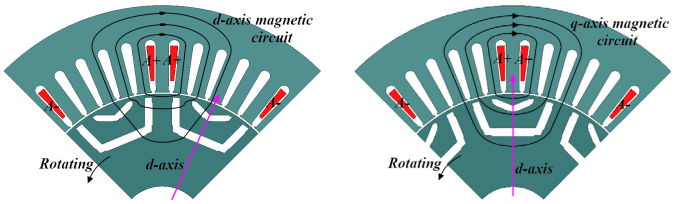

Fig. 2. Equivalent armature reaction magnetic circuit of proposed IPM machine. (a) *d*-axis. (b) *q*-axis.

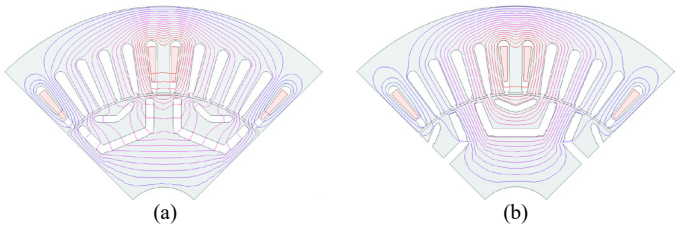

Fig. 3. Armature reaction magnetic flux lines of proposed IPM machine. (a) *d*-axis. (b) *q*-axis.

can be found that the *d*-axis armature reaction magnetic circuit coincides with the main PM field magnetic circuit. However, the *q*-axis magnetic circuit flows through the interval gap of PM layer. It is worth noting that the direction of q-axis magnetic circuit contributes the reluctance torque of IPM machine directly. Thus, it can be anticipated that the reluctance torque of IPM machines can be improved based on the optimization of the *q*-axis magnetic circuit.

Fig. 3 depicts the *d*-*q* axis armature reaction magnetic flux lines based on finite-element method (FEM). It should be noted that only *q*-axis armature current is injected to obtain *q*-axis armature reaction magnetic field. Similarly, only *d*-axis current is injected for *q*-axis armature reaction magnetic field. Since only the armature reaction magnetic field is considered, the rotor PMs is removed purposely. When the *d*-*q* axis magnetic circuit is separated, shown in Fig. 3, its corresponding magnetic circuits are symmetrical. Because the magnetic resistance of the *d*-axis magnetic path is large, only a little magnetic flux lines are able to pass through the magnetic circuit of the d-axis. In contrast, due to small *q*-axis magnetic resistance, it can be seen more magnetic flux lines pass through the *q*-axis magnetic circuit. Comparing the Fig. 2 and Fig. 3, it can be seen that the result of FEA and theoretical analysis are consistent in a sense the *d*-axis magnetic circuit does pass through PMs, while the *q*-axis magnetic circuit does not have any magnetic barriers.

By using FEM, the calculated *d*- axis and *q*-axis inductances with *d*-*q* axis current are shown in Fig. 4, where small circle denotes under the no-load and rated operating modes. In Fig. 4, it can be shown that when the *d*-axis and *q*-axis stator armature currents are small, the IPM machine consists of a large *d*-axis and *q*-axis inductance. It is because the resistance of the armature reaction magnetic circuit increases along with the current significantly.

III. Performance Comparison

The proposed IPM machine is designed and compared with four existing models, as presented in Fig. 5. The PM usage of different IPM machines is listed in Table II. It should be noted

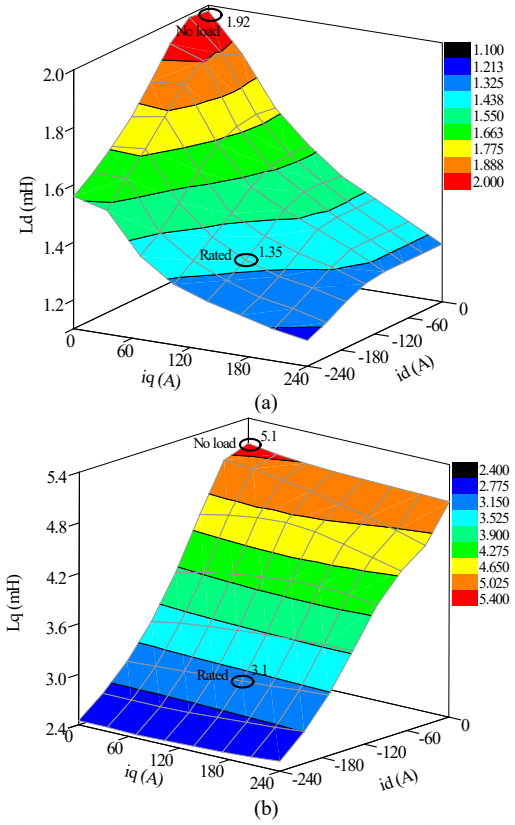

Fig. 4. Inductances of proposed IPM machine. (a) *d*-axis. (b) *q*-axis.

that the no-load magnetic fluxes are superimposed to illustrate the leakage of IPM machine with different rotor structures. The IPM machines are operated under the rated condition with the speed equals to 600r/min with current as 236A. All of the IPM machines have been optimized, while their key machine parameters are tabulated in Table I. For a fair comparison, all these machines are developed with same size, slot filling factor, electromagnetic loading, material and operating environment.

A. Back-EMF

It is well known that the amplitude of back-EMFs is closely related to the no-load PM magnetic field. Fig. 5 illustrates the no-load magnetic flux lines. In Fig. 5, it can be found that all these rotor topologies have serious inter-polar magnetic flux linkage. Moreover, it can be seen clearly that the topology I does not have any magnetic congregate effect. On the other hand, the topologies II, III and IV have an excellent magnetic congregate effect, where it is the main disadvantage of IPM machines.

For EVs machines, excessive PM magnetic field ends up with a lot of influence on main circuit when machine is stopped quickly or in idle running. To reduce this risk and to retain the scope of security, the maximum back-EMF so as the PM magnetic field should be limited. Therefore, relatively low back-EMFs are suitable for EV applications. To minimize the torque pulsation, the back-EMF harmonics should be reduced during the development processes. Fig. 6 compares the back-EMFs of all proposed machines. Obviously, all the obtained waveforms are very non-sinusoidal. It is shown the existing IV IPM machine consists of the largest back-EMF among the group, and it should be able to generate a larger PM torque. However, a high PM magnetic field is disadvantageous

for EVs machines. Conversely, both of the proposed and existing III IPM machines consist of relatively lower back-EMFs. In particular, the existing I machine consists of the lowest back-EMF while the existing II machine of the second. It reduces the existence of PM field that produces a safety issue effectively and improves the reliability of the machine.

TABLE I
MAIN PARAMETERS OF IPM MACHINES

Symbol	Quantity	Value
D_s	Outer stator diameter (mm)	264
D_o	Inner stator diameter (mm)	161.9
L	Axial length of stator core (mm)	50.17
h_{PM}	PM thickness	8/6
p	Number of poles	8
N_s	Number of stator slots	48
g	Airgap length (mm)	0.73
P	Rated output power (kW)	72
m	Number of phase	3
B_r	Remanence of PM (T)	1.2
	PM material	NdFe35H
	Iron core lamination	50WW465
n	Rated speed (rpm)	600
I	Rated current (A)	236

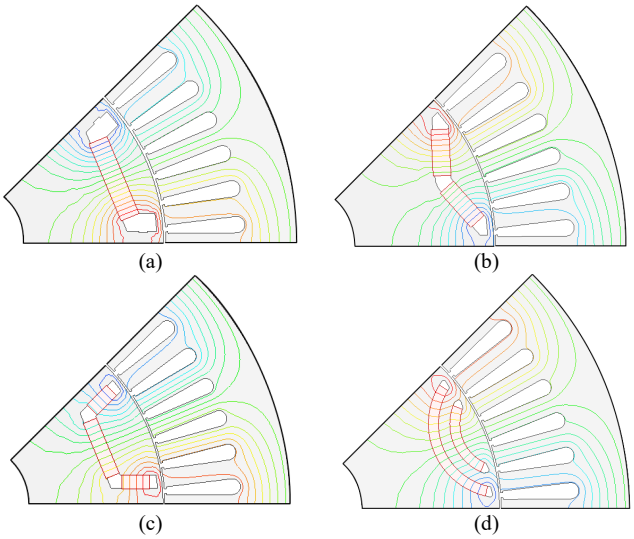

Fig. 5. Five different IPM machines. (a) Existing I. (b) Existing II. (c) Existing III. (d) Existing IV.

TABLE II
PM USAGE OF DIFFERENT IPM MACHINES (kg)

Existing I	Existing II	Existing III	Existing IV	Proposed
0.094	0.095	0.10	0.12	0.11

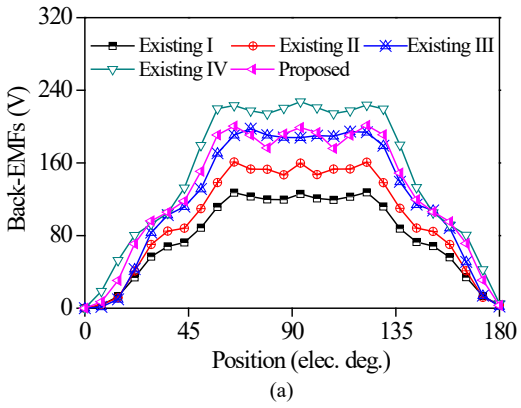

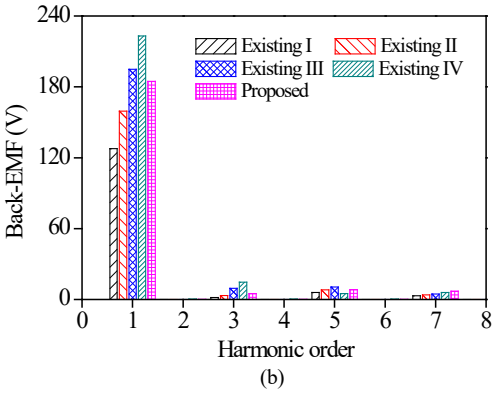

Fig. 6. Back-EMFs. (a) Waveforms. (b) Spectrum.

B. Inductance

Since the permeability of rotor PMs is smaller than that of iron core, the q-axis inductance is larger than d-axis inductance for IPM machines. This is the reason why the IPM machines have a bigger saliency ratio than its surface PM counterparts. The impact of magnetic saturation on inductance makes their values become not inconstant but vary with d-q axis current. The d- and q-axis inductances can be calculated as:

$$L_d = \frac{\lambda_d - \lambda_{PM}}{I_d}\Bigg|_{i_q=0} \tag{1}$$

$$L_q = \frac{\lambda_q}{I_q}\Bigg|_{i_d=0} \tag{2}$$

where λ_{PM} is the flux linkage generated by PM field and λ_d is the d-axis flux linkage generated by armature reaction field. The FEA-calculated d- and q-axis inductances are shown in Fig. 7. It can be observed that the value of d-q axis inductances is greatly influenced by the armature reaction of magnetic field. Generally, the impact of magnetic armature reaction on inductance makes q-axis current become greater than d-axis current. Furthermore, the proposed IPM machine suffers from the influence of armature reaction of magnetic field slightly [15], [16]. Also, the proposed IPM machine consists of a larger difference between d- *and* q axis than its counterparts.

Fig. 8 compares the saliency ratio of these five IPM machines at no-load and rated operation. It can be seen that the saliency ratio of each machines is not constant under different operation modes. In other words, rotor structure is not the only factor affecting the saliency ratio, while the armature reaction of magnetic field should be the other one. Therefore, it can be

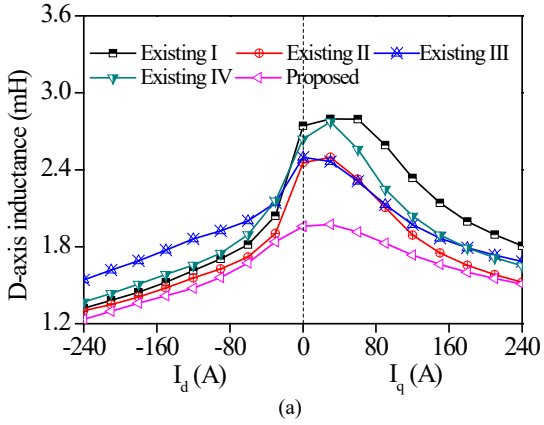

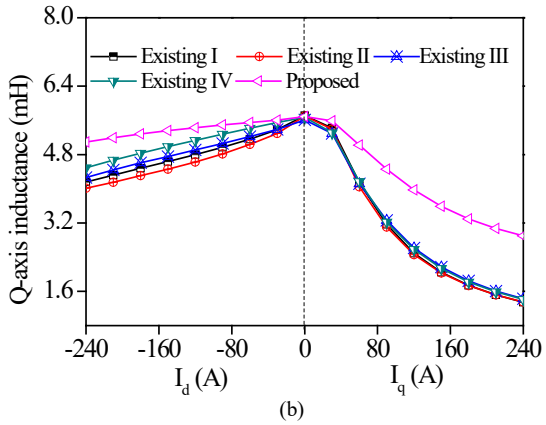

Fig. 7. *d*-*q* axis inductances. (a) *d*-axis. (b) *q*-axis.

found that the proposed rotor topology consists of the largest saliency ratio within the group, and it is a very important indicator for the reluctance torque. Hence, it is believed to achieve a better torque performance so as flux-weakening capability than the other four IPM machines.

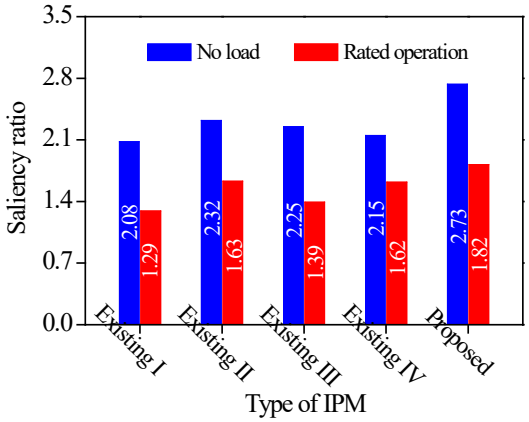

Fig. 8. Comparison of saliency ratios.

C. Electromagnetic Torque

The electromagnetic torque of an IPM machine consists of two components, with complete different mechanisms. Namely, PM component is produced based on interaction between air-gap magnetic field and armature reaction magnetic field and the reluctance component is instead on asymmetry between the IPM machines magnetic circuit of *d*-axis and *q*-axis. The electromagnetic torque can then be defined as:

$$T_{em} = \frac{3p}{2}\left[\lambda_{pm}\cdot i_q + \left(L_d - L_q\right)\cdot i_d i_q\right] \tag{3}$$

where L_d and L_q are the *d*-*q* axis inductances, i_d and i_q are the *d*-*q* axis currents, respectively. The i_d and i_q are governed by:

$$\begin{cases} i_d = -I_s\cdot\sin(\gamma - 90^\circ) \\ i_q = I_s\cdot\cos(\gamma - 90^\circ) \end{cases} \tag{4}$$

where I_s is the space current vector, γ is the current vector angle and $-i_d$ represents the nature of demagnetization of *d*-axis armature reaction current. In order to maximize the electromagnetic torque, rational current vector angle should be adopted and different machines have different optimal current vector angles. Generally, for the IPM machines, the *q*-axis inductance is larger than *d*-axis inductance. In order to achieve the favorable reluctance torques, the current vector angles should be greater than 90° (electrical degree). In other words, the *d*-axis armature reaction of magnetic field complies with the nature of the demagnetization [5]. Fig. 9 compares the torques of all five IPM machines at the rated operations, where the current vector angle is 141°. It can be obtained that the existing IV candidate consists of the largest PM component, while the proposed IPM machine consists of the largest reluctance component. In particular, the reluctance torque of the proposed IPM machine accounts for 51.1% of its electromagnetic torque and this feature is very suitable for EVs [17]-[20].

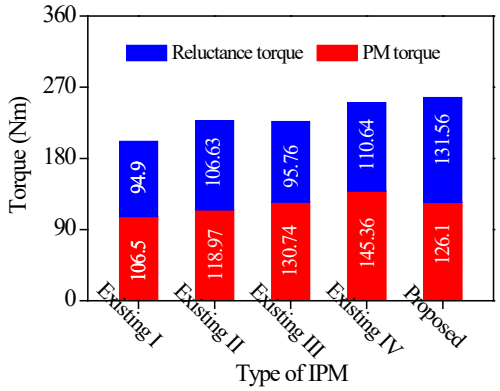

Fig. 9. Comparison of torques.

D. Flux-Weakening Performance

Fig. 10 presents the vector diagram of IPM machine. The maximum voltage supplied by the inverter to the PM machine is limited by the maximum bus voltage. The angular speed of the rotor is limited by the amplitude of the stator voltage vector of the IPM machine. The schematic diagram of flux weakening control is shown in Fig. 11. The voltage equation of IPM machines can be expressed as:

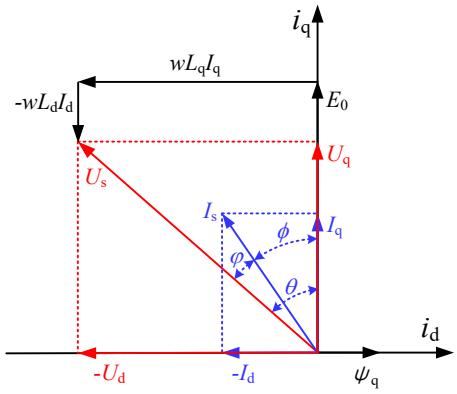

Fig. 10. Vector diagram of IPM machine.

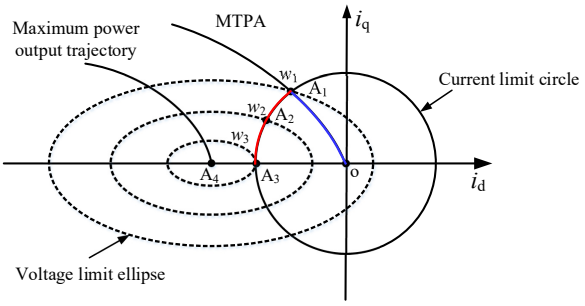

Fig. 11. Schematic diagram of flux weakening control.

$$u = \omega\sqrt{\left(\delta L_d i_q\right)^2 + \left(L_d i_d + \lambda_{PM}\right)^2} \tag{5}$$

where ω is the rotor angular velocity, and δ is the salient rate which is defined as:

$$\delta = \frac{L_q}{L_d} \tag{6}$$

Finally, the speed equation can be expressed as:

$$n = \frac{u_{\lim}}{p\sqrt{\left(\lambda_{PM} + L_d i_d\right)^2 + \left(L_q i_q\right)^2}} \tag{7}$$

It is known that the maximum speed depends on the voltage limitation of the power inverter and *d*-axis demagnetization current. When the voltage reaches a limited value, it is difficult to further increase the speed.

In order to achieve higher speed, the *d*-axis current should be demagnetized, and it is so-called as flux-weakening operation. When armature current is used entirely as a *d*-axis demagnetization current, the ideal maximum speed is then obtained. In that occasion, the maximum speed can be calculated as:

$$n_{\max} = \frac{u_{\lim}}{p\left(\lambda_{PM} + L_d i_{d\lim}\right)} \tag{8}$$

where i_{dlim} is the limit value of the *d*-axis demagnetization current. In other word, when the *q*-axis current becomes zero, the armature current is said to be demagnetized. The flux-weakening index is defined as the ratio of the rated current to the machine characteristic current, which can be expressed as:

$$\rho = \frac{L_d I_r}{\lambda_{PM}} \tag{9}$$

where I_r is the rated current. When the ρ is close to 1, the theoretical maximum operating speed can be increased to infinity [9]. The torque-speed characteristics of the IPM machines at the rated currents are plotted in Fig. 12. It can be seen that the proposed IPM machine have better flux-weakening capability than the other four IPM machines.

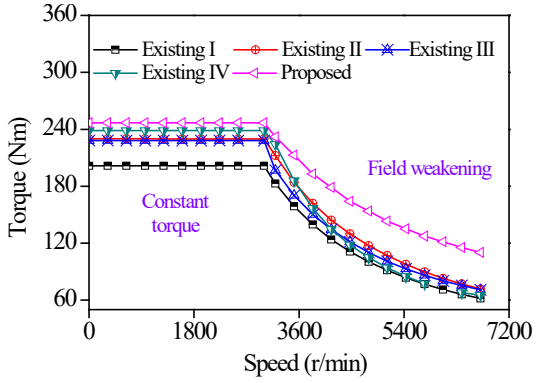

Fig. 12. Comparison of flux-weakening performances.

E. Overload Capability

In general, when the machines experience a circuit fault, its currents will increase significantly. This will lead to the magnetic circuit saturation and thereby deteriorate the output torque capability. Thus, overload capability is essential for EV applications. Fig. 13 compares the overload capabilities of the IPM machines and it can be shown the proposed IPM machine outperforms the most excellent overload capability than the other IPM machines. When the overload current reaches twice of its rated current, the proposed IPM machine is still able to achieve high torque capability.

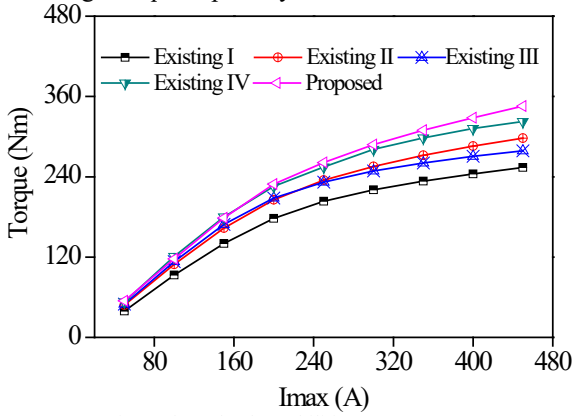

Fig. 13. Comparison of overload capabilities.

IV. Experimental Validation

In order to verify the electromagnetic performances, a 48s8p newly designed PM machine is built and the distributed windings are adopted. It should be noted that the PM machine is a present prototype. The photos of prototype machine and test platform are presented in Fig. 14. Both back-EMFs and torque measurements are carried out using the same torque sensor. Obviously, from Fig. 14(a), it can be observed that different PM modules are combined (Hybrid SPM and IPM).

The no-load back-EMFs of newly designed PM machine at FEM predicted and measured at the speed vary 0 to 1500 r/min is shown in Fig. 15. The result indicates that the FEM predicted and experimental is consistent. In other word, the experimental results are very reliable.

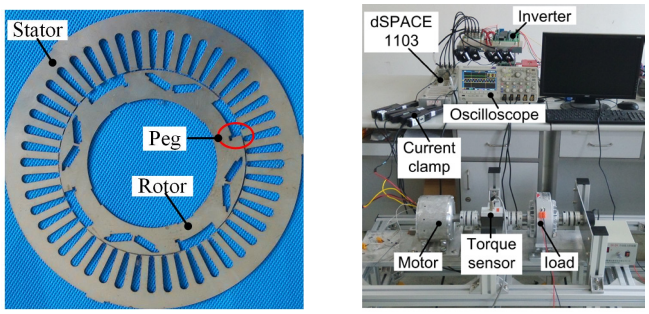

(a) (b)

Fig. 14. Prototype photos. (a) Stator and rotor core. (b) Platform.

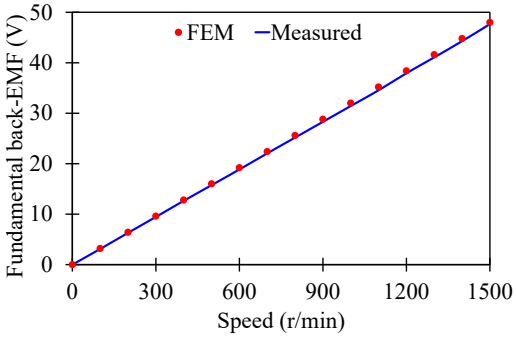

Fig. 15. No-load back-EMF.

Fig. 16 exhibited the torque performance of newly designed PM machine. It can be observed that, when the speed is less than 600 r/min, the PM machine works on the region of constant torque. Also, the output power reduces greatly at 600 r/min when the terminal voltage is given as a constant value of 35V. It can be concluded that the newly designed PM machine offers poor flux-weakening performance. This is because the rated current of the PM machine is much lower than the character current and the flux-weakening can be achieved in a small area. That is, when the speed is greater that 600r/min, the PM machine does not work in the flux-weakening region and its torque and power have a drop.

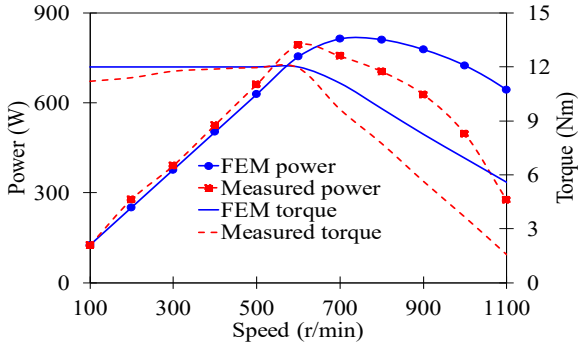

Fig. 16. Torque performance of newly designed PM machine.

V. Conclusions

In this paper, an IPM machine with new rotor topology has been proposed and the five different IPM machines are evaluated, particularly for EV applications. All IPM machines have been optimized to achieve high reluctance torques, while the proposed IPM machine has shown distinctive merits among its counterparts. In particular, it suffers very little from the influence of armature reaction of magnetic field and it can also provide the highest reluctance torque, which contributes 51.1% of its electromagnetic torque. Moreover, the proposed IPM machine is able to achieve an excellent flux-weakening performance and overload capability. To verify the proposed idea, an experimental setup of a 3-phase 48-slot and 8-pole hybrid rotor PM machine is established. It has been confirmed based on the PM optimization, IPM machines can provide a bright potential for EV applications.

References

[1] S. Li, D. Han and B. Sarlioglu, "Modeling of Interior Permanent Magnet Machine Considering Saturation, Cross Coupling, Spatial Harmonics, and Temperature Effects," *IEEE Trans. Transport Electrification*., vol. 3, no. 3, pp. 682-693, Sept. 2017.

[2] B. D. S. G. Vidanalage, M. S. Toulabi and S. Filizadeh, "Multimodal design optimization of V-shaped magnet IPM synchronous machines," IEEE Trans. Energy Convers., vol. 33, no. 3, pp. 1547-1556, Sep. 2018.

[3] R. Lin, S. D. Sudhoff and C. Krousgrill, "Analytical method to compute bridge stresses in V-shape IPMs," *IET Electric Power Applications*., vol. 12, no. 7, pp. 938-945, Aug. 2018.

[4] Y. Nie, I. P. Brown, and D. C. Ludois, "Deadbeat-direct torque and flux control for wound field synchronous machines," *IEEE Trans. Ind. Electron*., vol. 65, no. 3, pp. 2069-2079, Mar. 2018.

[5] S Duan, L Zhou and J wang, "Flux weakening mechanism of interior permanent magnet synchronous machines with segmented permanent magnets," *IEEE Trans. Appl. Supercond*., vol. 24, no. 3, p. 0500105, Jun. 2014.

[6] Z. Q. Zhu and B. Lee, "Integrated field and armature current control for dual three-phase variable flux reluctance machine drives," *IEEE Trans. Energy Convers*., vol. 32, no. 2, pp. 447-457, Jun. 2017.

[7] A. Wang, Y. Jia, and W. L. Soong, "Comparison of five topologies for an interior permanent-magnet machine for a hybrid electric vehicle," *IEEE Trans. Magn*., vol. 47, no 10, pp. 3606-3609, Oct. 2011.

[8] Z. Djelloul-Khedda, K. Boughrara, F. Dubas, A. Kechroud and B. Souleyman, "Semi-Analytical Magnetic Field Predicting in Many Structures of Permanent-Magnet Synchronous Machines Considering the Iron Permeability," *IEEE Trans. Magn*., vol. 57, no. 7, Jul. 2018, Art. ID 8103921.

[9] W. H. Kim, K. S. Kim, S. J. Kim, D. W. Kang, S. C. Go, Y. D. Chun, and J. Lee, "Optimal PM design of PMA-SYNRM for wide constant power operation and torque ripple reduction," *IEEE Trans. Magn*., vol. 45, no. 10, pp. 4660-4663, Oct. 2009.

[10] W. Q. Chu and Z. Q. Zhu, "Average torque separation in permanent magnet synchronous machines using frozen permeability," *IEEE Trans. Magn*., vol. 49, no. 3, pp. 549-555, Mar. 2013.

[11] F. R. Alam and K. Abbaszadeh, "Magnetic Field Analysis in Eccentric Surface-Mounted Permanent-Magnet Motors Using an Improved Conformal Mapping Method," *IEEE Trans. Energy Convers*., vol. 31, no. 1, pp. 333-344, Mar. 2016.

[12] S. H. Han, T. M. Jahns, W. L. Soong, M.K. Guven and M. S. Illindala, "Torque ripple reduction in Interior permanent magnet synchronous machines using stator with odd number of slots per pole pair," *IEEE Trans. Magn*., vol. 25, no. 1,pp. 118-127, March. 2010.

[13] A. R. Tariq, C. E. Nino-Baron and E. G. Strangas, "Iron and magnet losses and torque calculation of interior permanent magnet synchronous machines using magnetic equivalent circuit", *IEEE Trans. Magn*., vol. 46, no. 5, pp. 1205-1214, Jun. 2012.

[14] Q. Chen, G. Liu, W. Zhao, L. Sun, M. Shao and Z. Liu, "Design and comparison of two fault-tolerant interior-permanent-magnet motors," *IEEE Trans. Ind. Electron*., vol. 61, no. 12, pp. 6615-6623, Dec. 2014.

[15] H. Hwang, S. Bae and C. Lee, "Analysis and Design of a Hybrid Rare-Earth-Free Permanent Magnet Reluctance Machine by Frozen Permeability Method," *IEEE Trans. Magn*., vol. 52, no. 7, Jul. 2016, Art. ID 8106304.

[16] F. Chai, Y. Li, P. Liang and Y. Pei, "Calculation of the maximum mechanical stress on the rotor of interior permanent-magnet synchronous motors," *IEEE Trans. Ind. Electron*., vol. 63, no. 6, pp. 3420-3432, June. 2016.

[17] K. Yamazaki, and M. Kumagai, "Torque analysis of interior permanent magnet synchronous motors by considering cross magnetization: variation in torque components with permanent-magnet configurations," *IEEE Trans. Ind. Electron*., vol. 61, no. 7, pp. 3192-3201, Jul. 2014.

[18] Z. Yang, F. Shang, I. Brown, and M. Krishnamurthy, "Comparative study of interior permanent magnet, induction, and switched reluctance motor drives for EV and HEV applications," *IEEE Trans. Transp. Electrif*., vol. 1, no. 3, pp. 245-254, Oct. 2015.

[19] J. Zheng, W. Zhao, J. Ji, J. Zhu, C. Gu and S. Zhu, "Design to reduce rotor loss in fault-tolerant permanent-magnet machines," *IEEE Trans. Ind. Electron*., vol. 65, no. 11, pp. 8476-8487, Nov. 2018.

[20] G. Qi, J. T. Chen, Z. Q. Zhu, D. Howe, L. B. Zhou, and C. L. Gu, Influence of skew and cross-coupling on flux-weakening performance of permanent-magnet brushless AC machines," *IEEE Trans. Magn*., vol. 45, no. 5, pp. 2110-2117, May 2009.

Junqiang Zheng received the B.Sc. degree in electrical engineering from Jiangsu University, Zhenjiang, China, in 2014, where he is currently working toward the Ph.D. degree in electrical engineering. His research interests include machine design and electromagnetic field computation.

Wenxiang Zhao (M'08-SM'14) received the B.Sc. and M.Sc. degrees from Jiangsu University, Zhenjiang, China, in 1999 and 2003, respectively, and the Ph.D. degree from Southeast University, Nanjing, China, in 2010, all in electrical engineering. He has been with Jiangsu University since 2003, where he is currently a Professor with the School of Electrical Information Engineering. From 2008 to 2009, he was a Research Assistant with the Department of Electrical and Electronic Engineering, University of Hong Kong, Hong Kong. From 2013 to 2014, he was a Visiting Professor with the Department of Electronic and Electrical Engineering, University of Sheffield, Sheffield, U.K. His current research interests include electric machine design, modeling, fault analysis, and intelligent control. He has authored and co-authored over 130 technical papers in these areas.

Christopher H. T. Lee (M'12-SM'18) received the B.Eng. (First Class Honours) and Ph.D. degree in electrical engineering from Department of Electrical and Electronic Engineering, The University of Hong Kong, Hong Kong. He currently serves as an Assistant Professor in School of Electrical and Electronic Engineering, Nanyang Technological University, Singapore, and also a Visiting Scientist in Research Laboratory of Electronics, Massachusetts Institute of Technology, United States. His research interests include electric machines and drives, renewable energies, and electric vehicle technologies. In these areas, he has published about 60 technical papers.

Dr. Lee has received many awards, including Li Ka Shing Prize (the best Ph.D. thesis award) and Croucher Foundation Fellowship.

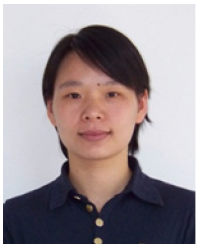

Jinghua Ji received the B.Sc., M.Sc., and Ph.D. degrees in electrical engineering from Jiangsu University, Zhenjiang, China, in 2000, 2003, and 2009 respectively. Since 2000, she has been with the School of Electrical and Information Engineering, Jiangsu University, where she is currently a Professor. From 2013 to 2014, she was a Visiting Scholar with the Department of Electronic and Electrical Engineering, University of Sheffield, Sheffield, U.K. Her areas of interest include motor design and electromagnetic field computation. She has authored and co-authored over 50 technical papers in these areas.

Gaohong Xu received B.Sc. in electrical engineering and automation and M.Sc. degree in power electronics and power drives from Jiangsu University, Zhenjiang, China, in 2009 and 2012, respectively. She is currently working toward the Ph.D. degree in Jiangsu University, Zhenjiang, China. Her current research interests include computation of electromagnetic fields for permanent-magnet machine and electric machine design.